Submitted to *Energy & Environmental*

Supporting Information

Fabricating high-energy quantum dots in ultra-thin $LiFePO_4$ nanosheet using a multifunctional high-energy biomolecule—ATP

Xudong Zhang,*[a] Zhiying Bi,[a] Wen He,*[a] Guang Yang,[c] Hong Liu[d] and Yuanzheng Yue*[ab]

X.Z., W.H. and Y.Y. designed the experiments. Z.B. performed experiments and calculations. H.L. and G.Y. assisted in the experiments. X.Z., W.H. and Y.Y. wrote the paper. All authors discussed the results and commented on the manuscript.

[a] *Institute of Materials Science and Engineering, Qilu University of Technology, Jinan 250353, China. Fax: +86 531 89631080; Tel: +86 531 89631518; *Corresponding author. *E-mail: zxd1080@126.com; hewen1960@126.com; yy@bio.aau.dk.*

[b] *Section of Chemistry, Aalborg University, DK-9000 Aalborg, Denmark.*

[c] *International Center for Dielectric Research, Xian Jiaotong University, Xian, 710049, China*

[d] *State Key Laboratory of Crystal Materials, Shandong University, Jinan 250100, China.*

Sections:

S1. Controlling growth of HEQDs

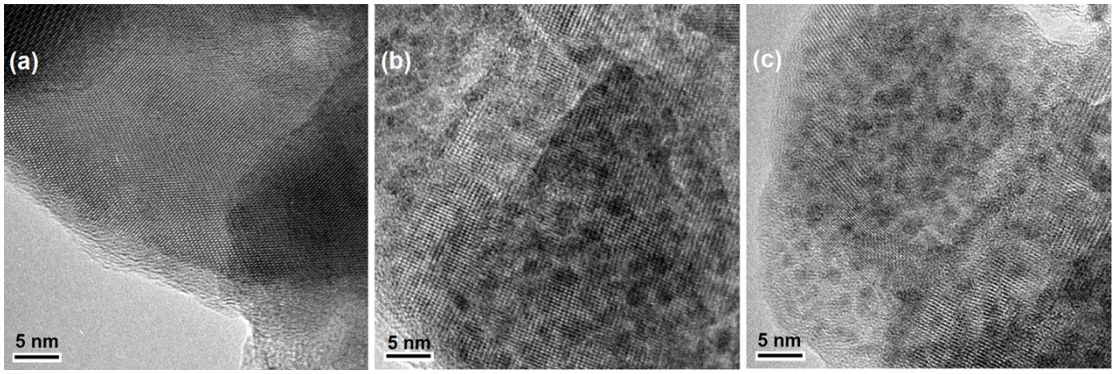

Fig. S1 HRTEM images of controlling growth of HEQDs. (a) MBCNW-LFP-HEQDs-1 sample prepared by using ATP biotemplate incubated for 30 min at 30 °C. (b) MBCNW-LFP-HEQDs-2 sample prepared by using ATP biotemplate incubated for 30 min at 40 °C. (c) MBCNW-LFP-HEQDs-3 sample prepared by using ATP biotemplate incubated for 30 min at 50 °C.

The average number, size and distribution of HEQDs in $LiFePO_4$ nanosheet can be controlled by changing the incubating temperature of ATP and growth time during the synthesized process. HRTEM image of MBCNW-LFP-HEQDs-1 sample synthesized by using ATP biotemplate incubated at 30 °C shows that no HEQDs were formed in its structure (Fig. S1a) because the high-energy phosphate bonds in ATP biomolecule were not release at all for interaction with Fe cations. The MBCNW-LFP-HEQDs-1 cathode delivered a lower discharge capacity of 106 mAh g^{-1} at 0.1 C (Fig. 6bA). Fig. S1b shows that more HEQDs were formed in the structure of MBCNW-LFP-HEQDs-2 sample synthesized by using ATP biotemplate incubated at 40 °C and its cathode delivered a higher discharge capacity of 197 mAh g^{-1} at 0.1 C (Fig. 6bB1). When the incubating temperature of ATP rises to 50 °C, Fig. S1c shows that the number of HEQDs decreased greatly in the structure of MBCNW-LFP-HEQDs-3 sample and the discharge capacity of its cathode at 0.1 C was reduced to 156 mAh g^{-1} (Fig. 6bC). The results indicate that HEQDs provide more storage sites of Li^+ ions and easier transfer kinetics of electrons and lithium ions, and displays the superior discharge capacity.

S2. High-resolution X-ray photoelectron spectrum (HRXPS) characterizations

Table S1. Fitted values of peak position based on P2p doublet and O1s for ULFPNP and MBCNW-LFP-HEQDs-2

Samples	P $2p_{1/2}$ (eV)	P $2p_{3/2}$ (eV)	Δ *(eV)	$O_1$1s (eV)	$O_2$1s (eV)	$O_3$1s (eV)
ULFPNP	134.3	133.7	0.5	531	531.8	532.7
MBCNW-LFP-HEQDs-2	134.3	131.8	2.5	526.8	531.1	533.4

S3. Structure characterizations

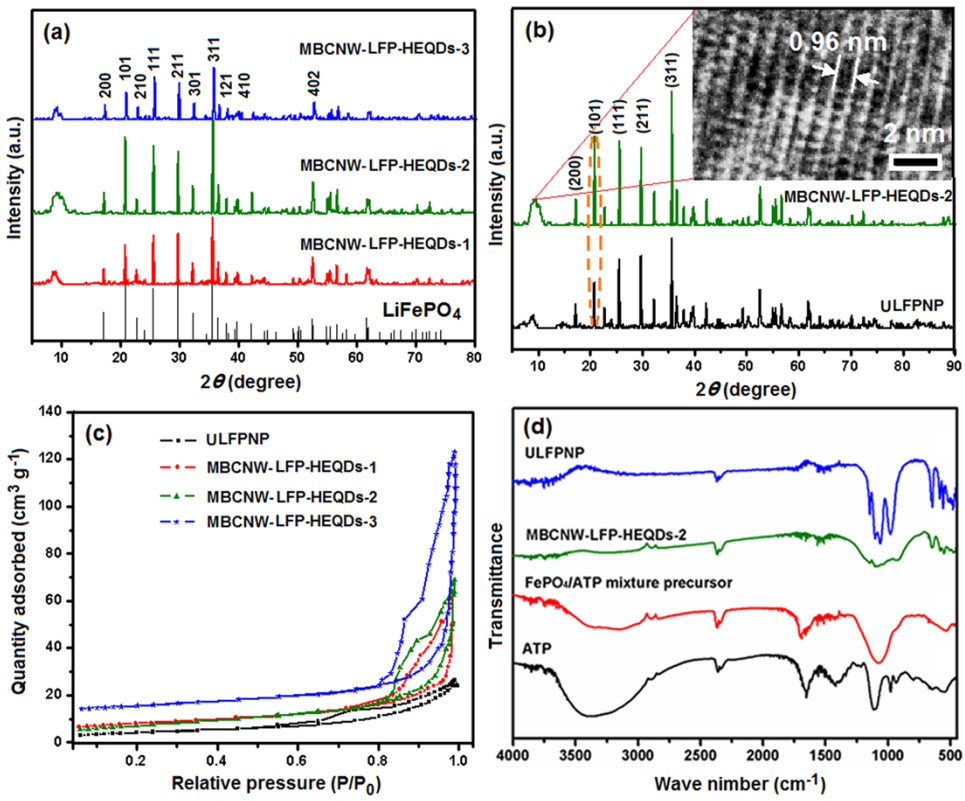

Fig. S2 Structure characterizations of the different samples. (a) XRD patterns of the different samples synthesizes at 700 °C. The peaks are indexed to the pure olivine ($LiFePO_4$) phase (JCPDS No.83-2092). (b) Comparison of XRD patterns and HRTEM image (inset) of MBCNW-LFP-HEQDs-2 synthesizes at 700 °C for 8h. (c) N_2 adsorption-desorption curves. (d) FTIR spectra of the different samples.

Fig. S2a shows the XRD patterns of samples synthesized at different conditions. The XRD results indicate that all of samples have orthorhombic olivine-type structure of pure phase $LiFePO_4$ (JCPDS No.83-2092) and there are no other diffraction peaks of any impurity phase,

and the residual carbon has an amorphous structure[1]. In the 2θ range of 8 to 12°, each XRD curve in Fig. S2a shows a wide and weak diffraction peak, which is assigned the layered structures with different interlamellar spacings in different samples. The HRTEM image of MBCNW-LFP-HEQDs-2 sample further confirms its layer structure with interlamellar spacing of 0.96 nm (inset in Fig. S2b). By comparing the XRD patterns of the different samples, the diffraction peak changes are seen. The diffraction peaks of the MBCNW-LFP-HEQDs-2 sample are stronger than that of other samples (Fig. S2a) and ULFPNP sample (Fig. S2b), implying a significant increase in crystallinity of the $LiFePO_4$ nanoparticles in MBCNW-LFP-HEQDs-2 sample through biomineralization processes. It's likely that the high-energy phosphate groups with negative charges in high-energy biomolecule ATP are not only the groups preferentially bonded with iron ions, but also the most important contributor to the free energy barrier for iron phosphate biomineralization at room temperature and pressure[2]. Besides, the (101) and (200) diffraction peaks of MBCNW-LFP-HEQDs-2 sample become stronger than that of ULFPNP sample, which indicates that the crystal growth of $LiFePO_4$ nanosheet is preferential in the [010] direction, resulting in increase of their crystallinity and distance of crystal faces and decrease of their strain (Table S2). This is attributed to different nucleation mechanism of ATP biomolecules. The summary of the structural features and performances for the MBCNW-LFP-HEQDs samples and ULFPNP sample is given in Table S2 and Table S3. The lattice volume of $LiFePO_4$ in the MBCNW-LFP-HEQDs-2 samples swells obviously than that of ULFPNP sample (Table S2a), because the in situ composite structure of HEQDs and active mesoporous biocarbon nanowires with $LiFePO_4$ nanoparticles leads to a distortion of $LiFePO_4$ crystal structure during heat treatment. The HEQDs and active mesoporous biocarbon nanowires play an important role in the enhancement of the electrical conductivity. To determine the carbon content of these composites elemental analysis has been performed using VarioEL IIICHN elemental analyzer

(Table S2d). The carbon content for MBCNW-LFP-HEQDs-2 sample is 12.85 wt%, causes a significant increase in rate capability and coulombic efficiency.

Table S2. Summary of the structural features and performances of the synthesized samples

Samples	V [a] [Å^3]	D_{211}[b] [nm]	D_{Li}[c] [cm^{2}s^{-1}]	C[d] [wt%]	R_0[e] [gcm^{-3}]	S[f] [m^{2}g^{-1}]	V_{meso}[g] [cm^{3}g^{-1}]	D_{pore}[h] [nm]	L_{P-O}[j] [Å]
ULFPNP	290.13	60.3	1.66×10^{-15}	1.807	4.270	13.70	0.0425	8.951	27.22
MBCNW-LFP-HEQD-1	291.43	66.4	8.16×10^{-16}	12.85	3.310	28.27	0.0766	22.01	26.24
MBCNW-LFP-HEQD-2	291.25	67.4	3.21×10^{-14}	12.85	3.885	26.66	0.0600	14.25	26.58
MBCNW-LFP-HEQD-3	290.96	66.7	4.75×10^{-16}	12.85	3.338	25.50	0.1459	22.29	26.34

[a] V: lattice volume of $LiFePO_4$ in the samples calculated by using Jade 5 XRD pattern-processing software. [b] D_{211}: crystallite size of $LiFePO_4$ estimated using Scherre's relation $t = 0.9\lambda / \beta_{1/2}\cos\theta$, where λ is the X-ray wave length, θ is the Bragg angle and β1/2 is the angular full-width-half maximum of the chosen (211) reflection in radian. [c] D_{Li}: lithium diffusion coefficients of the material estimated using electrochemical impedance. [d] C: carbon content determined by using Vario EL IIICHN elemental analyzer. [e] R_0: actual density calculated through pycnometer method. [f] S: specific surface area calculated through BET method. [g] V_{meso}: mesoporous volume. [h] D_{pore}: pore size. [j] L_{P-O}: P–O bond length calculated through using FTIR spectra.

Table S3. Summary of the structural features of the synthesized samples calculated by using Jade 5 XRD pattern-processing software

Samples	(hkl)	Distance of crystal face [Å]	Crystallite size [nm]	Crystallinity [%]	Strain [%]
ULFPNP	200	5.1496	70.3	95.85	-0.0374
	101	4.2681	66.9	90.52	
MBCNW-LFP-HEQD-1	200	5.1677	54.4	94.58	0.0151
	101	4.2737	55.3	85.42	
MBCNW-LFP-HEQD-2	200	5.1676	70.5	96.82	-0.0221
	101	4.2733	73.0	97.79	
MBCNW-LFP-HEQD-3	200	5.1541	62.1	95.03	-0.0196
	101	4.2727	68.6	91.89	

The mesopores participate in the charge storage processes but wide pathways, i.e. mesopores are necessary for a fast accessibility of ions. Due to the presence of mesopores, a carbon material can deliver a high energy at a high rate[3]. To obtain further information on the mesoporous structure of the samples, nitrogen adsorption measurements were performed. According to International Union of pure and Applied chemistry regulation[4], in Fig. S2c all the isotherm shapes of the samples are of the type-IV hysteresis loop pattern that indicates mesoporous characteristics. Barret–Joyner–Halenda pore-size-distribution curves of the samples see Fig S3. The MBCNW-LFP-HEQDs-2 sample shows the H3 hysteresis loop in the relative pressure (P/P_0) range of 0.80–0.98, representing a typical mesoporous feature caused

by nonuniform and open wormlike pores and the pore-size distribution centered at 14 nm (see Fig. S3). This is consistent with the HRTEM result, from which depicting the biocarbon nanowire morphology and mesoporous network structure can be recognized (see Fig. 4d). The pore structure data of the samples see Table S2f–h. Such an open interconnected mesoporous biocarbon nanowire network structure can significantly increase the permeability of the electrolyte and thus facilitate lithium ion diffusion.

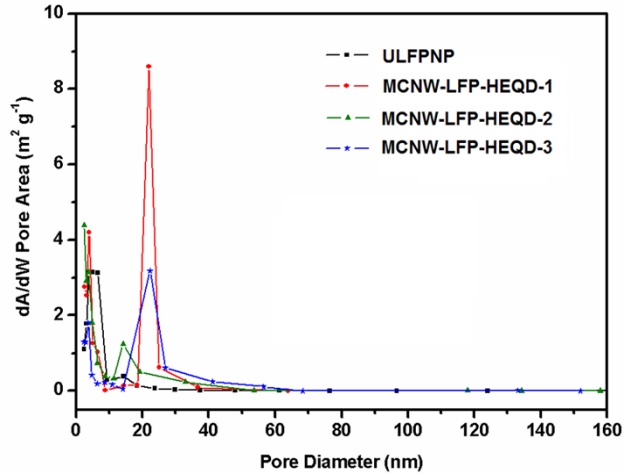

Fig. S3 Barret–Joyner–Halenda pore-size-distribution curves of the synthesized samples

In the synthetic process, the chemical bond linkages between ATP biomolecules with iron ions and the in situ nanocomposite linkages between $LiFePO_4$ nanosheets with the mesoporous biocarbon nanowire network were studied by FT-IR (see Fig. S2d). The FT-IR spectrum of pure ATP is shown in Fig.S2dA. The broad band at 3500 cm^{-1} is ascribed to the O-H stretching vibration of water. The dominant bands near 1692 and 1438 cm^{-1} are respectively assigned to amide I and amide II of the adenine proteins in ATP biomolecule. The band at 2890 cm^{-1} is derived from the CH_2 asymmetry stretching vibration of the adenine protein. The band at 1124 cm^{-1} is caused by the C-O stretching of carbohydrates found in the ribose._The broad band from 500 cm^{-1} to 800 cm^{-1} is ascribed to the vibration of the triphosphate part in ATP biomolecule [5,6]. Fig. S2dB shows the $FePO_4$/ATP mixture precursor. By comparing Fig. S2dA with Fig. S2dB, the following three changes are seen. First, the band near 1692 cm^{-1} has shifted to higher wavenumbers from pure ATP to $LiFePO_4$/yeast mixture

precursor and the band near 1124 cm^{-1} has shifted to lower wavenumbers. Second, the peak near 1438 cm^{-1} disappears and a new P-O band forms, which is ascribed to the ATP biomolecule binding with iron ions through an amine group and triphosphate. Finally, the band at 1045 cm^{-1} is enhanced due to the vibration superposition of the C-O and PO_4^{3-} groups and the band from 500 cm^{-1} to 700 cm^{-1} is weakened. These results indicate that hydroxyl (OH−) in the ribose and OPO_3^{2-} radicals in the triphosphate part play an important role in the chemical interaction between the ATP biomolecules and the iron ions. Fig. S2dD is the FT-IR spectrum of ULFPNP sample. The infrared spectral bands of $LiFePO_4$ are mainly distributed over two wavenumber ranges from 460 to 650 cm^{-1} and 940 to 1120 cm^{-1}. These bands respectively correspond to the internal stretching, internal bending and external oscillation modes of PO_4^{3-}. The band at 2375 cm^{-1} is due to the P-O stretching mode. The dominant bands from 940 cm^{-1} to 1040 cm^{-1} are due to PO_4^{3-}. The bands observed at 500–640 cm^{-1}, correspond to intramolecular symmetrical stretching vibrations of the Fe-O bond in the FeO_6 unit. By comparing Fig. S2dC with Fig. S2dD, two main changes are seen in the FTIR spectra. First, for the MBCNW-LFP-HEQDs-2 sample all the PO_4^{3-} bands have shifted to lower wavenumbers from those of ULFPNP sample. This result demonstrates an increase of the P-O chemical bond length and the high-energy phosphate bonds have been introduced in crystal structure of $LiFePO_4$ nanoparticles (Table S2jk). Second, the vibration transmittance of the PO_4^{3-} bands weakened. These changes indicate that there are in situ nanocomposit linkages between the $LiFePO_4$ nanoparticles and the mesoporous biocarbon nanowire coating network . Through the FT-IR spectroscopy results, we have verified that the deposition and self-assembly mechanism in Fig. 1 is feasible for synthetizing MBCNW-LFP-HEQDs.

S4. Lithium-ion diffusion coefficient studies

EIS is considered to be a powerful technique to evaluate the diffusion coefficient of lithium ion. This is because the Warburg impedance in the low frequency is directly related to the

lithiumion diffusion process in an electrode material.[3] To further understand the electrochemical behaviors of the the different samples, EIS measurements were carried out. In

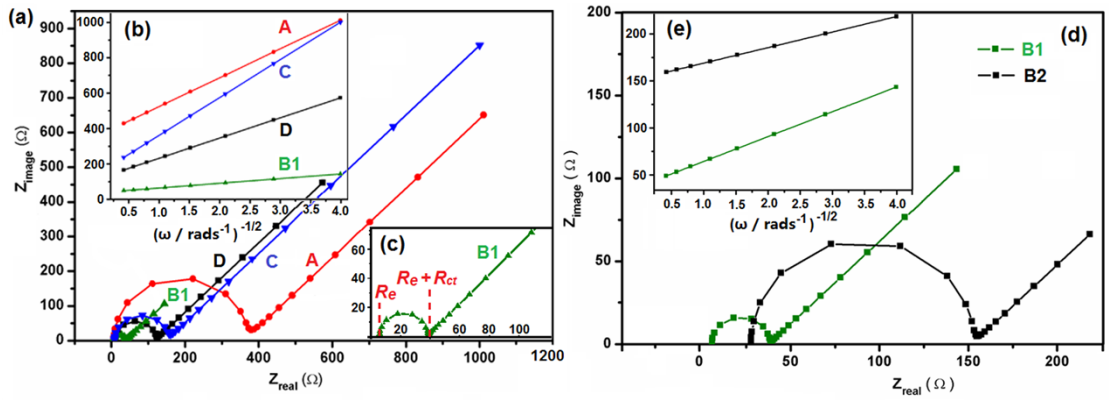

Fig. S4 Lithium-ion diffusion coefficient studies. (a) Nyquist plots of the different cathodes vs. Li anode to derive lithium chemical diffusion coefficient at room temperature. A is MBCNW-LFP-HEQDs-1 cathode; B1 is MBCNW-LFP-HEQDs-2 cathode; C is MBCNW-LFP-HEQDs-3 cathode and D is ULFPNP cathode. (b) The plots of impedance as a function of the inverse square root of angular frequency in the Warburg region in (a). (c) An enlarged Nyquist plot of the MBCNW-LFP-HEQDs-2 cathode vs. Li anode. (d) Nyquist plots of the MBCNW-LFP-HEQDs-2 cathode befor and after 100 cycles at 0.1 C at room temperature. (e) The plots of impedance as a function of the inverse square root of angular frequency in the Warburg region in (d).

Fig.S4a and S4d each EIS curve has an intersection with the Z_{real} axis, semicircles and an oblique line. The intercept in the high frequency region is related to the ohmic series resistance (R_e). It includes the interparticle contact resistance, electrolyte resistance and other physical resistances between the electrolyte and electrode. The radius of the semicircle at high frequency region on the Z′-axis is related to the charge transfer resistance (R_{ct}). The slope of inclined line in low frequency represents the Warburg impedance (W), which is associated with lithium-ion diffusion in $LiFePO_4$ cathode. The diffusion coefficient of lithium ion can be calculated from the plots in the low frequency region using the following equation:[7]

$$D = \frac{R^2 T^2}{2A^2 n^4 F^4 C^2 \sigma^2} \quad (1)$$

Where R is the gas constant, T is the absolute temperature, A is the surface area of the cathode, n is the number of electrons per molecule during oxidization, F is the Faraday constant (96, 486 $Cmol^{-1}$), C is the concentration of lithium-ion, and σ is the Warburg factor which obeys the following relationship:

$$Z_{real} = R_e + R_{ct} + \sigma\omega^{-1/2} \quad (2)$$

Where ω is angle frequency.

Fig.S4b shows the linear fitting of Z_{real} vs. $\omega^{-1/2}$, from which the slope σ can be obtained. Using this σ value it is possible to calculate the lithium diffusion coefficients of the material. The results showed that the lithium diffusion coefficient D_{Li} values of the ULFPNP and MBCNW-LFP-HEQDs-2 cathodes are 1.66×10^{-15}, 3.21×10^{-14} cm^2 s^{-1}, respectively (see Table S2c). Table S2c and Fig.S4d clear shows that the MBCNW-LFP-HEQDs-2 cathode has the biggest D_{Li} value and the smallest R_{ct} value (35Ω) because the mesoporous biocarbon nanowire networks provide high electric conduction for electron transfer. The D_{Li} value of the MBCNW-LFP-HEQDs-2 cathode after 100 cycles at 0.1 C reduced to 7.88×10^{-16} cm^2 s^{-1} and R_{ct} value increased to 125Ω (Fig.S4de) because of the mesoporous structure collapse. Thus, the D_{Li} and R_{ct} values indicate that the electrochemical kinetics of MBCNW-LFP-HEQDs-2 cathode is easier with Li^+ extraction than ULFPNP cathode. Furthermore, MBCNW-LFP-HEQDs-2 cathode has a higher slope of the inclined line in low frequency, indicating lower Warburg impedance. This means that lithium ion movements are rapider in the MBCNW-LFP-HEQDs-2 electrode than in the ULFPNP electrode. HEQDs can improve the lithium ion diffusion rate through abundant pathways in crystal structure of ultra-thin $LiFePO_4$ nanosheet. It leads to enhanced discharge capacity of MBCNW-LFP-HEQDs-2 electrode. Results of EIS tests indicate that the MBCNW-LFP-HEQDs-2 electrode has the lowest charge transfer resistance, and its electrochemical kinetics is easier regarding Li^+ extraction than that of the ULFPNP blank electrode. This is attributed to excellent nanocomposite of ultra-thin $LiFePO_4$ nanosheet particles with HEQDs embedded inside its crystal structure and mesoporous biocarbon nanowire coating that is formed in situ on the surface of nanosheet particles (Fig. 4acd).

Fig. S5a shows the cyclic voltammetry (CV) curves of MBCNW-LFP-HEQDs-2 electrode at different scanning rates. The well defined sharp redox peaks in the range of 3.2 V–3.8 V should be attributed to the Fe^{2+}/Fe^{3+} redox couple reaction, corresponding to lithium extraction and insertion in $LiFePO_4$ crystal structure. The slow scan rate 0.1 mV s^{-1} reveals an oxidation peak at 3.52V and a reduction peak at 3.32V, clearly demonstrating the presence of a reversible redox reaction that can contribute to Li^+ ion storage capacity. Even at the high scanning rate of 1.0 mV s^{-1} and after (B2) 100 cycles at 0.1 C (Fig. S5b), the sharp redox reaction peaks are still maintained. The contrast analysis in Fig. S5c and Fig. S5d has further

to confirm the outstanding reversibility of the lithium extraction/insertion reactions in the MBCNW-LFP-HEQDs-2 electrode. This result is consistent with the cycle stability performance of the materials as demonstrated in Fig.6d.

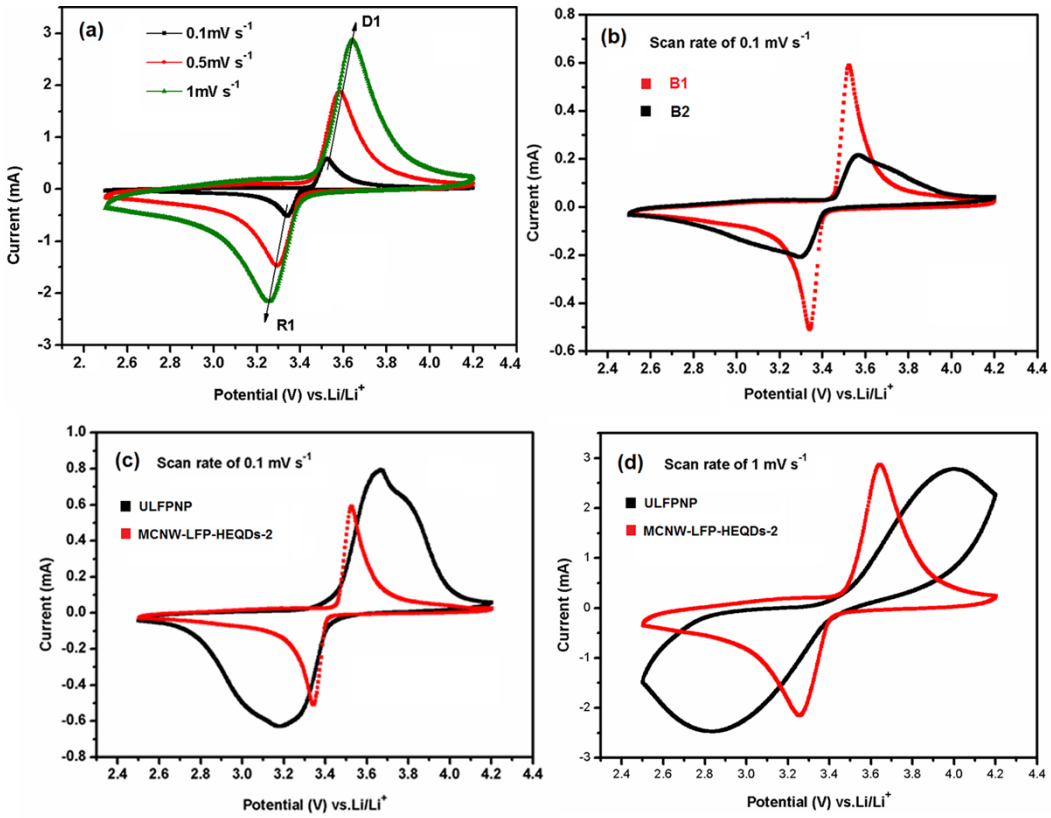

Fig. S5 (a) Cyclic voltammetry (CV) curves of MBCNW-LFP-HEQDs-2 electrode at different scanning rates. (b) CV curves at 0.1mV s^{-1} scanning rates for the MBCNW-LFP-HEQDs-2 cathodes befor (B1) and after (B2) 100 cycles at 0.1 C. (c) CV curves of different electrodes at 0.1mV s^{-1} scanning rates.. (d) CV curves of different electrodes at 1mV s^{-1} scanning rates.

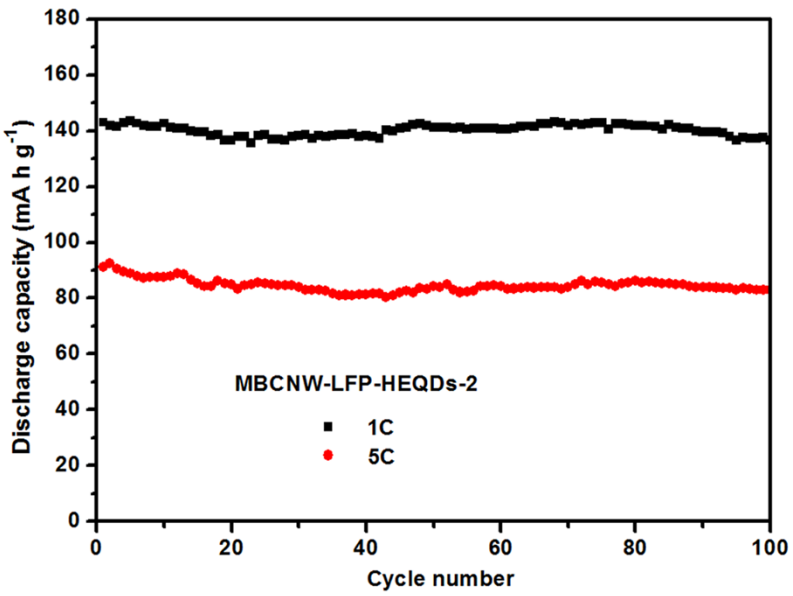

Fig. S6 Capacity retention of MBCNW-LFP-HEQDs-2 cathode for 100 cycles at different rate.

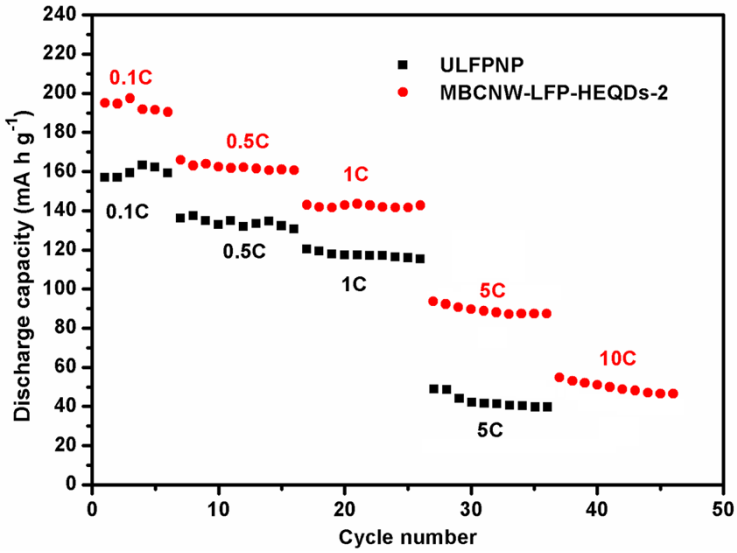

Fig. S7 Capacity retention of MBCNW-LFP-HEQDs-2 and ULPNP cathodes for 46 cycles at different rates..

References

1 X. G. Zhang, X. D. Zhang, W. He, Y. Z. Yue, H. Liu and J. Y. Ma, *Chem. Commun.*, 2012, **48**, 10093.

2 X. D. Zhang, W. He, Y. Z. Yue, R. M. Wang, J. X. Shen, S. J. Liu, J. Y. Ma, M. Li and F. X. Xu, *J. Mater. Chem.*, 2012, **22**, 19948.

3 X. Y. Du, W. He, X. D. Zhang, Y. Z. Yue, H. Liu, X. G. Zhang, D. D. Min, X. X. Ge and Y. Du, *J. Mater. Chem.*, 2012, **22**, 5960.

4 R. R. Xu, W. Q. Pang, J. H. Yu, Q. S. Huo and J. S. Chen, Chemistry-Zeolites and Porous Materials, Science Press, 2004, 146–158.

5 H. B. Ren and X. P. Yan, *Talanta* , 2012, **97**, 16.

6 J. H. Choy, S. Y. Kwak, J. S. Park and Y. J. Jeong, *J. Mater. Chem.*, 2001, **11**, 1671.

7 Y. Cui, X. L. Zhao and R. S. Guo, *Electrochim. Acta*, 2010, **55**, 922.